ANNALS OF PHYSICS 172, 419–450 (1986)

Anisotropic Honeycomb Domain Wall Networks in Uniaxial Systems

HYUNGGYU PARK, EBERHARD K. RIEDEL, AND MARCEL DEN NIJS

Department of Physics, University of Washington, Seattle, Washington 98195

Received February 11, 1986

A systematic study of the possibility of weakly incommensurate phases with a honeycomb domain wall network structure in uniaxial systems is presented. Competition between breathing entropy, the energy needed to tilt a domain wall, and the core energy of intersections can stabilize honeycomb phases in uniaxial systems. Two types of honeycomb networks are introduced, O-shaped and X-shaped. Breathing entropy turns out to be much weaker, compared to meander entropy, in uniaxial systems than in isotropic ones. Still, our study suggests that at the chiral melting transition the commensurate solid melts into an incommensurate fluid with a local short ranged O-shaped network order. Moreover, breathing entropy of X-shaped honeycomb networks might change the Pokrovsky–Talapov nature of the commensurate to striped incommensurate solid transition.

1. INTRODUCTION AND SUMMARY

Commensurate–incommensurate (CI) phase transitions in 2-dimensional systems have been investigated intensively in recent years, both theoretically [1–18] and experimentally [19–30]. Many of the theoretical predictions are detailed, but hard to verify experimentally, because the domain wall picture which underlies most of the theoretical studies only applies to the so-called weakly incommensurate (IC) phase, where the walls are well separated in units of the wall width. For example, in physisorption the domain walls seem to have a typical width of 20 to 30 Å [7–9, 23]. Therefore the monolayer is only weakly incommensurate at densities less than a few percent above the commensurate (C) density. The monolayer could skip the weakly IC phase altogether, by means of a first-order CI transition with a jump in density of a few percent. This might be the case for the uniaxial herringbone-ordered monolayer of N_2 on graphite [20, 21].

On the other hand, the domain wall theory, although detailed in its predictions, is far from complete. Several aspects have not been studied yet in a systematic way. The aspect which we address in this paper, is whether it is possible that in uniaxial systems honeycomb IC (HIC) phases exist intermediate between the C phase and the striped IC (SIC) phase. This is the first systematic study of this possibility. Most numerical studies were not tuned to observe an incommensurability in both directions, or simply did not look for it.

0003-4916/86 $7.50

595/172/2-12

An intermediate HIC phase is unlikely in uniaxial systems from an energetical point of view. Compared to the SIC structure, walls need to be tilted away from the preferred uniaxial direction and to intersect. However, entropy is the trademark of domain wall theories. As pointed out by Villain [1, 5], honeycomb networks have a powerful type of entropy associated with breathing modes. He showed that in isotropic systems breathing entropy stabilizes the intermediate HIC phase, between the C and SIC solid phases, at all temperatures, even if the intersection energy is positive. One cannot rely on energetics to denounce HIC phases, and should consider their presence in uniaxial systems as well.

In uniaxial systems the honeycombs will be narrow, with a very small tilt angle θ, see Fig. 1. In the anisotropic HIC phase the monolayer will be incommensurate in both directions, but the incommensurability in the uniaxial direction will be much smaller and probably difficult to detect. Whether the monolayer actually compresses in the uniaxial direction as well, depends on the details of the displacement vectors of the domain walls (see Sect. 2).

The purpose of this paper is to obtain insight into the interplay between entropy and energy in domain wall networks; breathing and meander entropy versus the energy of a domain wall in the uniaxial direction, the energy to tilt it, and the intersection energy. This study is only qualitative. We generalize Villain's theory for isotropic systems to uniaxial systems. It will be followed up, later, by detailed quantitative (numerical) calculations.

Our central result is that breathing entropy is very small compared to meander entropy in uniaxial systems. This is different from isotropic systems, where at low temperatures breathing entropy dominates over meander entropy. The origin of this difference is the tilt free energy of the domain walls. In isotropic systems all walls of the honeycombs follow easy directions, but in uniaxial systems walls must be tilted away from the uniaxial direction to form a network. Meander entropy dominates the temperature dependence of the tilt free energy and, thereby, indirectly the breathing entropy.

We focus on two types of honeycomb networks. They are labeled *OH* and *XH* to reflect their shapes, see Fig. 1. The *OH* phase turns out to be stable at high temperatures only and may not exist as a solid but only as a fluid (see Sect. 3 and 4). The origin of this is that in the *OH* network the tilted walls cannot be of the same type as the vertical walls (see Sect. 2). The *XH* phase is the true generalization of the isotropic HIC phase. It contains only one type of domain wall (see Sect. 2) and extends all the way to zero temperature between the C and SIC solid phases, but is extremely narrow (Sect. 5). Each of the two networks has possible implications on a different aspect of the theory of CI transitions.

The *OH* phase has implications for chiral melting. Many of the theoretical predictions only apply when the IC phase can be described by one type of domain wall. The chiral 3-state Potts model [11–18] is one of the simplest models that include more than one type of domain wall. In the region where both wall types are important, beyond the so-called Lifshitz point, the C solid might melt directly into an IC fluid. The difference in structure between the IC fluid at the chiral melting

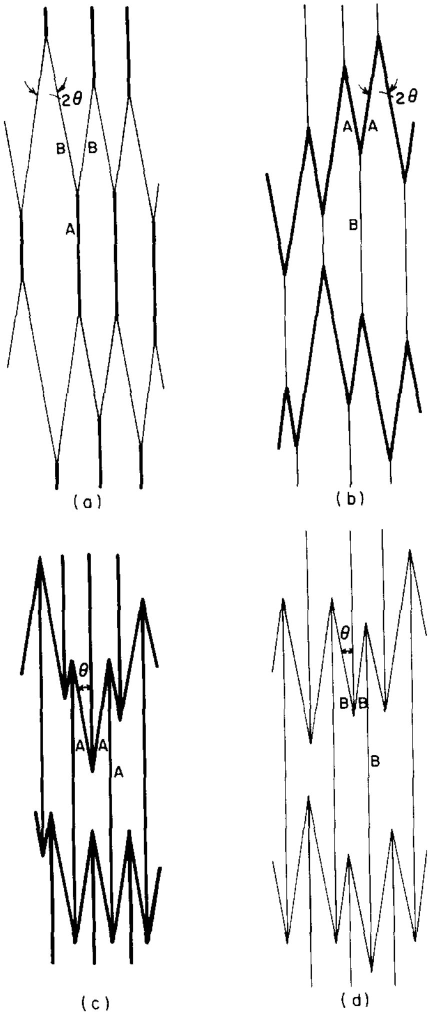

FIG. 1. Four types of honeycomb networks: (a) *OH*1, (b) *OH*2, (c) *XH*1, and (d) *XH*2. The heavy lines represent domain walls of type A and the light lines walls of type *B*.

transition and the SIC fluid at the other side of Lifshitz point, is the basic unresolved question. Our calculation suggests that the *OH* structure is the backbone of the IC fluid at the chiral melting transition. The *OH* phase appears in our phase diagram precisely there where chiral melting should take place in more sophisticated treatments. The *OH* phase is only stable beyond a multicritical point, which we associate with the Lifshitz point. If the *OH* network is indeed the backbone of the chiral fluid, the IC fluid will be incommensurate in both directions, in a narrow intermediate region beyond the chiral melting line before becoming a SIC fluid.

The *XH* phase has implications for the C to SIC phase transition, which is generally believed to be a Pokrovsky–Talapov (PT) transition [4]. Our calculation opens the possibility of a new type of C to SIC transition. Strictly speaking, in our phase diagram the C and SIC phases are not even adjoining. In analogy to Villain's theory for isotropic systems, our generalization predicts the presence of an intermediate *XH* phase between the C and SIC solids extending to zero temperature. However the *XH* phase is extremely narrow and probably will not survive more detailed quantitative studies; except, of course, when the intersection energy is negative. Still, breathing entropy challenges the PT nature of the C to SIC transition. The *XH* network is a dislocation network from the point of view of the SIC phase (see Sect. 2). The (almost) stability of the *XH* phase indicates a softness of the SIC phase with respect to the formation of local clusters of *XH*-type dislocation networks. Breathing entropy compensates for the core energy of the dislocations even when this energy is large. Therefore, compared to the domain wall density, the dislocation density may become large on approach of the C–SIC transition. The PT theory assumes a low dislocation density. In the language of renormalization theory, the PT fixed point is located at zero dislocation density and its crossover exponent in the direction of finite dislocation density is irrelevant. The breathing entropy argument indicates that there is possibly a crossover to a new type of C–SIC transition fixed point at large dislocation density.

To summarize our results: The tilt energy of domain walls causes the breathing entropy to be small compared to the meander entropy in anisotropic HIC phases. Therefore those HIC phases are not as stable as the ones in isotropic systems where the breathing entropy is much more powerful. However, the *OH* and *XH* networks have possible implications for the nature of the chiral melting and the PT transition in uniaxial systems. This warrants that our qualitative theory presented here be followed up by detailed (numerical) quantitative calculations.

The outline of this paper is as follows. In Section 2, we describe the energetics and the topological aspects of domain walls, introduce the *OH* and *XH* types of domain wall networks, and discuss the chiral 3-state Potts model. In Section 3, we generalize and analyze Villain's theory for isotropic HIC phases to anistropic *OH*-type networks, assuming that the walls are rigid. In Section 4, we include meander entropy into the description of the *OH* network. In Section 5, we repeat the entire procedure for the *XH* phase, and present a comparison with the isotropic case.

2. TOPOLOGICAL RULES AND ENERGETICS OF DOMAIN WALL NETWORKS

In this section we describe the topological and energetical aspects of domain walls, discuss the two types of honeycomb domain wall networks, comment on the relation between domain wall theories and experimental realizations of IC phases in, e.g., physisorbed monolayers, and discuss the relationship with the chiral 3-state Potts model.

A weakly IC monolayer is described by domains, where the monolayer is com-

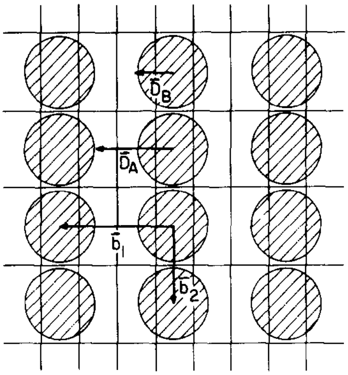

FIG. 2. Commensurate (3×1) structure. $\mathbf{D}_A$ and $\mathbf{D}_B$ denote the displacement vectors of the superheavy and the heavy walls, respectively, while $\mathbf{b}_1$ and $\mathbf{b}_2$ are the lattice vectors of the commensurate monolayer.

mensurate with the substrate periodicity, separated by domain walls. The domain walls carry the excess monolayer particles. Domain wall theories describe the monolayer by the excitations of the domain walls. All fluctuations at length scales smaller than the domain wall width are integrated out, and incorporated in the energy parameters of the walls. Several types of domain walls are possible, depending on the symmetry and the degeneracy of the nearby C ground states. Besides its width l_W, each type of domain wall is characterized by its direction, denoted by a unit vector $\hat{d}$ orthogonal to the wall, and its displacement vector $\mathbf{D}(i, j)$. Only the energetically most favorable walls need to be considered. In the uniaxial systems discussed here the energetically most favorable walls follow the uniaxial direction or are only slightly tilted relative to that direction.

The displacement vector $\mathbf{D}(i, j) = -\mathbf{D}(j, i)$ of the wall is a lattice vector of the substrate. It measures the displacement of the atoms in domain j on one side of the wall with respect to the atoms in domain i across the wall, sec e.g., Fig. 2. At each point where walls meet and/or transform into different types the total sum of displacement vectors must be zero modulo a lattice vector $\mathbf{b}_i$ of the C monolayer. For example, at the intersection points in Fig. 3a, a vertical wall V splits into a right-tilting wall R and a left-tilting wall L such that

$$\mathbf{D}_V(i, j) + \mathbf{D}_R(j, k) + \mathbf{D}_L(k, i) = \mathbf{0} \ (\mathrm{mod}\ \mathbf{b}_i). \tag{1}$$

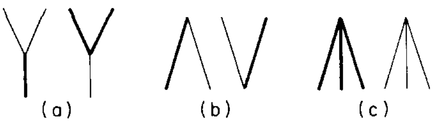
(a) (b) (c)

FIG. 3. Transformations between domain wall types: (a) intersections in OH networks, (b) domain wall pair creations and annihilations, and (c) intersections in XH networks.

When the contour integral is not equal to zero, but equal to a C monolayer lattice vector $\mathbf{b}_i$, the intersection is called a dislocation. Dislocation-intersections will, in general, induce more local strain and therefore have a larger intersection energy, because they create extra rows of monolayer atoms. This does not imply, however, that dislocation networks are less favorable, because also the wall energy must be taken into account.

The energy per unit length of a wall of type A is composed of two contributions: the elastic energy C_A due to the compression of the monolayer inside the wall and the adsorption energy μ_A of the excess particles:

$$\begin{aligned} E_A &= C_A(\hat{d}_A, \mathbf{D}_A, l_{w_A}) - \mu_A(\mathbf{D}_A, \hat{d}_A), \\ \mu_A &= n\,\mu^{(p)}\mathbf{D}_A \cdot \hat{d}_A, \end{aligned} \tag{2}$$

where $\mu^{(p)}$ is the adsorption energy per particle and n the monolayer density of the C ground state. Notice that the energy changes sign when $\mu^{(p)}$ increases. The CI transition is driven by the type of walls whose energy becomes negative first. Only those walls and other nearby low-cost walls need to be considered.

Consider first the network of Fig. 1a. Assume that the vertical walls are of the type labelled A. To form the network, the tilted walls must be of a different type. The displacement vectors of the tilted walls are prescribed by (1). If the intersection in Fig. 1a are not dislocations, i.e, if the contour integral (1) is equal to zero, and if the left and the right tilting walls are of the same type, labeled B, then it follows from (1) and (2) that $\mu_B = \mu_A/2$. This is obviously correct in the limit of zero tilt where the honeycombs are very narrow. It is also correct at finite tilt angles if one measures the wall length by its projection along the uniaxial directions, as we will do. The energies of these types of walls can be expanded in the tilt angle,

$$\begin{aligned} E_A(\theta) &= C_A + \tfrac{1}{2}C''_A \tan^2(\theta) - 2\mu, \\ E_B(\theta) &= C_B + \tfrac{1}{2}C''_B \tan^2(\theta) - \mu. \end{aligned} \tag{3}$$

The subscript B on $\mu_B = \mu_A/2$ is dropped for convenience. The compression energies C_A and C_B, and the tilt energies C''_A and C''_B must be considered to be temperature dependent. Equation (3) exhibits the proper θ dependence: at finite temperatures the tilt energy is not linear in the tilt angle, as $|\tan(\theta)|$, but quadratic. This is due to meander entropy, and explained in Section 4. The A-type walls are more favorable than the B-type walls if $C_A < 2C_B$.

Consider the networks shown in Figs. 1b–d. Because of the nature of the A and B walls specified in (3), these are dislocation networks. The network in Fig. 1a will be called *OH*1 (*O*-shaped). The dislocation network in Fig. 1b, where the roles of the A and B walls are reversed, will be referred to as *OH*2. Notice that *OH*2 is only allowed if $2\mathbf{D}_A - \mathbf{D}_B$ is equal to a lattice vector of the C monolayer.

At first sight it appears that the X-shaped honeycomb networks in Figs. 1c–d can be ignored, because the angles at the intersections are very sharp and must lead to large intersection energies. However, these networks are constructed from one type of walls only; in contrast to the *OH*-type networks all wall energies at zero tilt are equal. This aspect will turn out to be more important than the magnitude of the intersection energies. The dislocation network in Fig. 1c will be called *XH*1 and the one of Fig. 1d, *XH*2. Notice that *XH*1 (resp. *XH*2) is only allowed if $\mathbf{D}_A$ (resp. $\mathbf{D}_B$) is equal to $\frac{1}{3}$ of a lattice vector of the C monolayer $\mathbf{b}_i$ or a multiple of that, see (1).

Each type of the intersections, see Fig. 3, has a core energy associated with it. The intersection energies in our four networks will be denoted I_{O1}, I_{O2}, I_{X1}, and I_{X2}.

It is useful to keep in mind a simple example like a 3×1 system, where the monolayer has three C ground states, and where the *A*-type walls are usually called the superheavy walls and the *B*-type walls the heavy walls [12], with the displacement vectors pointing in the direction orthogonal to the uniaxial direction and with $\mathbf{D}_B = \mathbf{D}_A/2 = \mathbf{b}_1/3$ (see Fig. 2). All four networks of Fig. 1 are allowed in this and other uniaxial systems with three C ground states, like H, O, or H_2O on Ni(110) and H on Fe(110) [26–29].

However the results of this paper apply to a wider class of adsorbed monolayers. In an attempt to describe an actual experimental system by the domain wall theory, and to check whether one or more HIC phases are allowed, one has to follow the following steps. First, the nearby C ground state with respect to which the domain walls are to be defined has to be identified. Next, using the symmetries and degeneracy of this C ground state, all possible types of domain walls can be characterized. Then, one must hope that the available knowledge about the microscopic interactions is sufficient to identify the energetically most favorable types of domain walls. It is also important to determine the typical domain wall width, because that sets the experimental density interval where the results of the domain wall theory might apply. Finally, it can be checked whether these walls obey the topological rules outlined above.

For example, in systems like N_2, CO, ortho-H_2, or ethane physisorbed on graphite, the isotropy of the substrate is spontaneously broken by the orientational ordering of the molecular axes of the monolayer molecules [20, 21, 24, 25]. In N_2 on graphite [20, 21] the C positional order is the well known $\sqrt{3} \times \sqrt{3}$ structure, but the degeneracy of the C ground state is larger than three and the system behaves uniaxial, because of the herringbone type of the orientational order. These systems have more than two types of walls, including ones that obey the topological rules for *OH* and/or *XH* phases. However, it is not easy to make definite predictions, because especially for these systems it is difficult to estimate the wall energies accurately.

Intermediate HIC phases cannot be realized in systems with only two degenerate ground states, e.g., Xe on Cu(110) [30], the ANNNI model [2], because it takes at least three colors to color a HIC network. Such monolayers can still become incommensurate in both directions, but only at monolayer densities which are high relative to the domain wall width, i.e., where the monolayer floats and the domain wall picture does not apply.

This study also addresses the chiral 3-state Potts model. This model was introduced by Ostlund [11] and has been studied extensively in recent years

[12–18]. It serves as a prototype model to study chiral melting [17], the possibility of a direct melting of the C phase into an IC fluid in the presence of two types of domain walls. The chiral 3-state Potts model describes a system with three C ground states. Its two types of walls are known as clockwise and anti-clockwise walls, and are associated with the superheavy and heavy walls in a monolayer with a (3×1) C ground state, and with our A and B walls. Consider a rectangular lattice with lattice constants $a_\perp$ and $a_\parallel$. Choose $a_\perp$ and $a_\parallel$ of the same order of magnitude as the domain wall width. Each cell contains many monolayer atoms. A Potts variable $\phi = 0, \pm 2\pi/3$ is assigned to each $a_\perp \times a_\parallel$ cell; to represent the three possible C positions of the monolayer inside the cell. In the conventional version of the chiral 3-state Potts model, only nearest neighbor interactions are taken into account:

$$H = -\sum_{\langle n,m\rangle} \left[J\cos\left(\phi_{n+1,m} - \phi_{n,m} - \tfrac{2}{3}\pi\Delta\right) + J'\cos\left(\phi_{n,m+1} - \phi_{n,m}\right)\right]. \tag{4}$$

In this model description the domain walls follow the bonds of the lattice. The wall energies of the A and B walls at zero tilt angle are given as

$$\begin{aligned} E_A(0) &= J\left[\cos\left(\tfrac{2}{3}\pi\Delta\right) - \cos\left(\tfrac{2}{3}\pi(1-\Delta)\right)\right], \\ E_B(0) &= J\left[\cos\left(\tfrac{2}{3}\pi\Delta\right) - \cos\left(\tfrac{2}{3}\pi(1+\Delta)\right)\right]. \end{aligned} \tag{5}$$

The chirality parameter Δ plays the role of the chemical potential. The non-chiral Potts model is located at $\Delta = 0$, the energy of the A walls changes sign at $\Delta = \frac{1}{2}$, and the energy of the B walls at $\Delta = -\frac{1}{2}$. Compare this with (3), where the wall energies become equal at $\mu = C_A - C_B$, the energy of the A walls changes sign at $\mu = C_V/2$ and that of the B walls at $\mu = C_B$. Notice the periodicity in Δ, which is absent in (3). Because the model has only nearest neighbor interactions, the intersection energies I_O and I_X are equal to zero. Another special aspect of the conventional chiral Potts model is that the tilt energies are equal, $C''_{\mathrm{A}} = C''_{\mathrm{B}}$.

Figure 4 shows the phase diagram of the chiral 3-state Potts model as it is conventionally drawn [13, 17, 18]. One of the unresolved issues is the presence and nature of a so-called chiral melting transition along the line between the Potts critical point P (where the wall energies are equal, $E_A(0) = E_B(0)$) and the so-called Lifshitz point L. Below L one expects a direct transition between the C and SIC solid phases described by the Pokrovsky–Talapov theory [4]. The SIC phase contains only A walls (or only B walls, depending on which are the energetically most favorable walls). The melting of the SIC phase is believed to be Kosterlitz–Thouless like. The Lifshitz point is the boundary between the regions where the system realizes that there are two types of wall, and where it ignores the unfavorable type. This is the most likely structure of the phase diagram as concluded from earlier studies; but there are a lot of question marks. There is strong numerical evidence for the existence of the Lifshitz point [13, 14, 18], but also evidence that P and L merge in the limit of large dislocation core energy [15, 16]. Our study, although

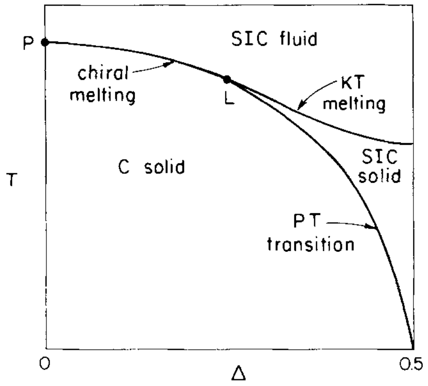

FIG. 4. Conventional phase diagram for the 3-state chiral Potts model. P is the nonchiral Potts melting point and L the Lifshitz point.

phenomelogical in nature, gives new insight into this problem, because it approaches this model from a new perspective. Earlier studies did not address the possibility of the HIC phases in uniaxial systems.

3. *OH*-TYPE HONEYCOMB NETWORKS OF RIGID DOMAIN WALLS

In this section Villain's theory [1, 5] for isotropic HIC phases is generalized to uniaxial systems and applied to the *OH*-type phases. The walls are assumed to be rigid. In Section 4 their meander entropy is included. The *XH*-phases are ignored momentarily. They are discussed in Section 5. Strictly speaking the results of this section only apply to very low temperatures, because only the breathing entropy is accounted for. Other types of entropy due to, e.g., meander excitations, imperfections in the network (dislocations), and local fluctuations in the angles of the honeycombs are not included explicitly. To some extent these other types of entropies only renormalize the wall energy parameters C_A and C''_A, see (3), and also the intersection energies I_0. Instead of treating these parameters as constants, one might introduce ad hoc temperature dependencies to represent those other entropies, and deform the phase diagrams accordingly. In Section 4, meander entropy is incorporated explicitly, and indeed its major effect is to renormalize the wall energy parameters (meander entropy is proportional to the wall length). However some of those entropies introduce phase transitions; dislocations lead to (IC) fluids. Fluid phases are not established in our phase diagrams, because dislocations are not treated explicitly.

The central question of this section is whether an intermediate *OH* phase can be realized in uniaxial systems at the onset of incommensurability between the C and SIC solid; whether the breathing entropy is able to compensate the increase in energy needed to transform a striped structure into a *OH* network like in isotropic systems. Breathing entropy competes with the energy needed to transform a piece of vertical wall into two vertical walls of the tilted type, the energy needed to tilt these walls, and the intersection energy.

In hexagonal domain wall networks, breathing deformations of the hexagons conserve the total wall length in each of the three directions V, L, and R (see Fig. 5). When the honeycombs are large enough such that the wall–wall interactions can be neglected, i.e., that the only energies in the problem are the wall energy per unit length and the intersection energy, then the breathing excitations conserve the total energy. This configurational degeneracy is called breathing entropy [5]. Figure 5 shows that breathing entropy is not special to isotropic networks, where the three inside angles of the honeycombs, θ_V, θ_R, and θ_R are equal. It is also present when these angles are different.

For isotropic honeycombs, Villain [5] showed that all honeycomb network configurations can be generated by breathing semi-regular networks, where all honeycombs are identical, see Fig. 6. Each semi-regular network can be labeled by the lengths of the three honeycomb sides and three inside angles. The partition function reduces to a sum over all possible semi-regular networks, weighted by the number of irregular network configurations associated with each semi-regular network. Villain constructed an approximation for this weight function. In Appendix A we generalize his result to uniaxial systems where the honeycombs are very anisotropic with small top angle θ_V.

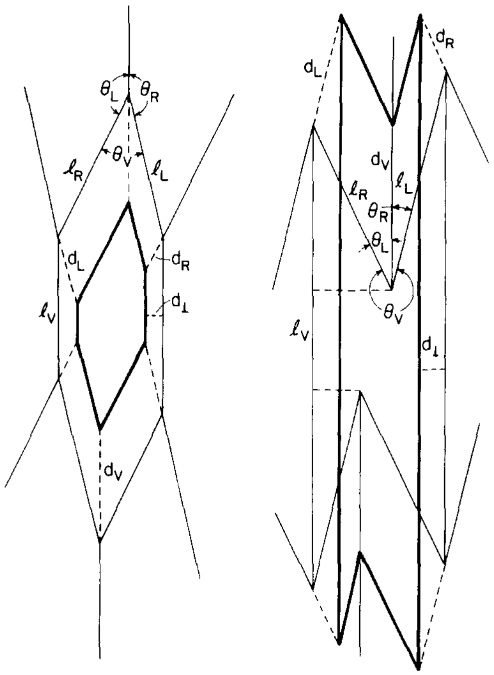

(a) (b)

FIG. 5. Breathing modes in OH and XH networks.

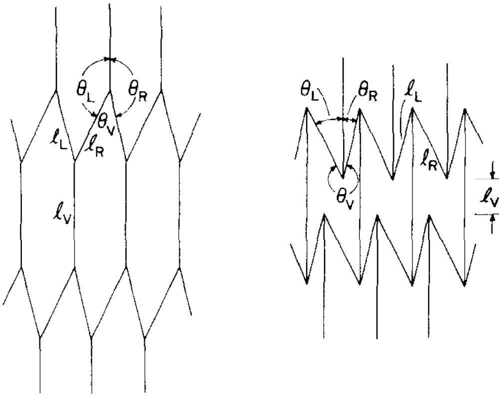

(a) (b)

FIG. 6. *OH* and *XH* semi-regular honeycomb networks.

To count the breathing modes a cutoff must be introduced. In Section 4 the meander entropy of the walls is included by assuming that the walls follow locally the bonds of a cutoff lattice. In this section the walls are still rigid, but can rotate by continuous angles. We introduce the cutoff by requiring that the intersection points of the honeycombs coincide with lattice points of the cutoff lattice. This lattice should not be confused with that of the substrate periodicity. Its lattice constants are comparable with the domain wall width, in physisorption typically of the order of 20–30 Å and much larger than the substrate periodicity. The symmetries of the monolayer and substrate determine the choice of the cutoff lattice. For example, for Kr on graphite it would be honeycomb or triangular, and for H on Fe(110) rectangular. In uniaxial systems it can always be chosen to be rectangular; e.g., in N_2 on graphite at temperatures below its orientational melting transition (at higher temperatures the cutoff lattice must be triangular or honeycomb). For convenience, we choose a rectangular cutoff lattice and label its lattice constants in the directions orthogonal and parallel to the uniaxial direction by $a_\perp$ and $a_\parallel$.

The approximation for the breathing entropy per semi-regular honeycomb network configuration is obtained in Appendix A. For convenience we will assume that the R and L walls are of the same type. Then the network has reflection symmetry, i.e., $l_R = l_L$ $(= l_T)$ and all angles are determined by the tilt angle θ as: $\theta_V = 2\theta$ and $\theta_R = \theta_L = \pi - \theta$. See Fig. 6 for the definitions of the angles and lengths of the honeycombs. Then

$$S_{\text{breath}} = -\nu \ln\left[g\, a_\perp \left(\frac{1}{l_T \sin(\theta)} + \frac{1}{l_V \tan(\theta)} \right) \right], \tag{6}$$

where g is a constant of order of unity, and ν is the total number of honeycombs,

$$\nu = \frac{A}{2\, l_T \sin(\theta)[l_V + l_T \cos(\theta)]}, \tag{7}$$

with A the total substrate area.

Consider the $OH1$ network of Fig. 1a. The free energy per unit area of a semi-regular network with sides l_T and l_V and tilt angle θ is given as

$$f(l_T, l_V, \theta) = \frac{1}{2l_T \sin(\theta)[l_V + l_T \cos(\theta)]} \left[2I_{O1} + l_V E_A + 2E_B(\theta)\, l_T \cos(\theta) \right.$$
$$\left. + k_B T \ln\left[g\, a_\perp \left(\frac{1}{l_T \sin(\theta)} + \frac{1}{l_V \tan(\theta)} \right) \right] \right], \tag{8}$$

where I_{O1} is the intersection energy of the walls in the $OH1$ network. The tilt angle θ is treated as an order parameter, like the wall lengths l_T and l_V. This implies that local fluctuations in θ are neglected. The values of the three order parameters are determined by minimizing the free energy. It is convenient to redefine them as

$$\begin{aligned} S_T &= l_T \sin(\theta), \\ S_V &= l_V \tan(\theta), \\ \varphi &= \tan(\theta), \end{aligned} \tag{9}$$

and to redefine the coupling constants as

$$\begin{aligned} a &= E_A(0)/k_B T = (C_A - 2\mu)/k_B T, \\ b/2 &= E_B(0)/k_B T = (C_B - \mu)/k_B T, \\ c &= C''_B/k_B T, \\ d &= 2I_{O1}/k_B T + \ln(g\, a_\perp), \end{aligned} \tag{10}$$

see (3) and (5). If in addition we measure the free energy density f in units of $k_B T$, then (8) simplifies to

$$f(S_T, S_V, \varphi) = \frac{\varphi}{2\, S_T(S_T + S_V)} \left[a\, S_V/\varphi + b\, S_T/\varphi + c\varphi\, S_T + d + \ln\left(\frac{1}{S_T} + \frac{1}{S_V} \right) \right]. \tag{11}$$

This is a valid approximation only when S_T and S_V are large with respect to the lattice cutoff $a_\perp$. The free energy of the $OH2$ phase is also given by (11), but with different values of the coupling constants

$$\begin{aligned} a &= E_B(0)/k_B T = (C_B - \mu)/k_B T, \\ b/2 &= E_A(0)/k_B T = (C_A - 2\mu)/k_B T, \\ c &= C''_A/k_B T, \\ d &= 2I_{O2}/k_B T + \ln(g\, a_\perp). \end{aligned} \tag{12}$$

In the chiral 3-state Potts model, see (4) and (5), the tilt energies of the *OH*1 and *OH*2 phases are equal, $C''_A = C''_B$, and the intersection energies are equal to zero, $I_{01} = I_{02} = 0$.

Typical phase diagrams are shown in Fig. 7. In Fig. 7a the *A* walls are more favorable than the *B* walls by choosing $C_A < 2C_B$, see (3); in Fig. 7b the *B* walls are more favorable; and Fig. 7c shows the phase diagram in the chiral 3-state Potts model language. An intermediate *OH* phase is indeed present between the C and SIC phases, but, contrary to the isotropic case, the *OH* phase does not extend all the way down to zero temperature, but only exists above a multicritical point *L*.

At the point *L* in Fig. 7a the SIC and C phases coexist with the *OH*1 phase; not with the *OH*2 phase. The fact that the *A* walls are energetically more favorable than the *B* walls ($C_A < 2C_B$) does not imply that the *OH*1 phase must appear at *L*. The *OH*2 phase would appear, if the ratio $x = S_T/S_V$, which characterizes the ratio

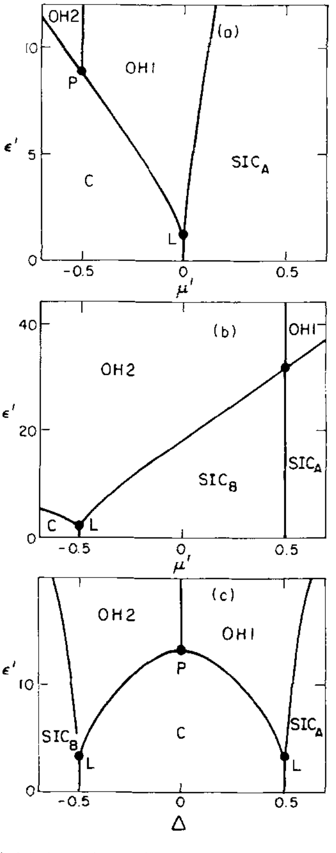

FIG. 7. Phase diagram in the rigid domain wall approximation: (a) for $C_A < 2C_B$, (b) for $C_A > 2C_B$, and (c) for the 3-state chiral Potts model. SIC$_A$ is the striped incommensurate phase with *A*-type domain walls and SIC$_B$ with *B*-type domain walls. Temperatures and chemical potentials are shown in the units of $\varepsilon' = \varepsilon/[(2eg)^2(2C_B - C_A)]$ and $\mu' = (\mu - C_A/2)(2C_B - C_A)$ in (a); $\varepsilon' = \varepsilon/[(2eg)^2(C_A - 2C_B)]$ and $\mu' = (\mu - C_A/2)/(C_A - 2C_B)$ in (b); and $\varepsilon' = \varepsilon/[J(2eg)^2]$ in (c). In (a) and (b) $C''_A = C''_B$ and $I_{01} = I_{02} = 0$.

between the tilted and vertical wall lengths, is larger than $\frac{1}{2}$. In the rigid wall approximation x is always smaller than $\frac{1}{2}$ at L, but in Section 4 where meander entropy is included, x will become larger than $\frac{1}{2}$ and the $OH2$ phase will appear instead of the $OH1$ phase.

Within this approximation, the droplet excitations are absent in the C solid phase, and its free energy $f_{\mathrm{C}} = 0$. The SIC phase is not well represented since meander excitations are not included yet. The SIC phase is close-packed, with a wall along every vertical bond, and free energy $f_{\mathrm{SIC}} = a$. The OH phases correspond to non-trivial minima of the free energy with respect to the three order parameter variables S_T, S_V, and φ:

$$\begin{aligned} \varphi/S_V &= a - b + c\varphi^2, \\ \varphi/S_T &= \frac{(3c\varphi^2 - b)(a - b + c\varphi^2)}{(2a - b + c\varphi^2)}, \\ 2c\varphi S_T &+ d + \ln(1/S_V + 1/S_T) = 0, \end{aligned} \tag{13a}$$

and with free energy

$$f = \frac{1}{2}\left[\frac{a}{S_T} - \frac{\varphi}{S_V(S_V + S_T)}\right]. \tag{13b}$$

These equations are solved numerically for temperature T and chemical potential μ or chirality Δ, using (10) and (12).

At the C-OH phase boundary the free energy of the OH phases is equal to zero. This determines the phase boundary and the values of the order parameters

$$\begin{aligned} a &= \frac{S_T\,\varphi}{S_V(S_V + S_T)}, \\ b &= \frac{(S_V - S_T)\,\varphi}{2(S_V + S_T)\,S_T}, \\ c &= \frac{1}{2\,\varphi\,S_T}, \\ d &= -1 - \ln(1/S_T + 1/S_V). \end{aligned} \tag{14}$$

The transition is first-order, like in the isotropic case. The jumps in the order parameters and the location of the C-OH phase boundary can be rewritten more explicitly as

$$\begin{aligned} 2bx^2 + ax - a &= 0 \qquad (x = S_T/S_V), \\ S_V &= (2ac(1 + x))^{-1/2}, \\ \varphi &= (2cxS_V)^{-1}, \\ ac &= \frac{x^2}{2(1 + x)^3}\exp[-2 - 2d]. \end{aligned} \tag{15}$$

The phase boundaries of the SIC phase are not well represented, because of the close packed nature of this phase in this approximation. The C–SIC phase transition at $a = 0$ is first order, but will become second-order after meander entropy is included, in section 4. The HIC-SIC transition is also first order, and will remain so after meander fluctuations are included.

The presence of the multicritical point L is the most important aspect of this calculation. L is located at

$$\begin{aligned} a &= 0, \\ 4bc &= \exp[-2-2d]. \end{aligned} \tag{16}$$

Near L the OH phase looks very striped like; as illustrated by the jump in the order parameters along the C–OH phase bounary in the vicinity of L,

$$\begin{aligned} S_V &\sim (2ac)^{-1/2}, \\ S_T &\sim (4bc)^{-1/2}, \\ \varphi &\sim (b/c)^{1/2}. \end{aligned} \tag{17}$$

On approach of L the top angle of the honeycombs remains finite, and also the width $2S_T$ of the honeycombs remains finite, but the vertical wall length diverges.

As functions of temperature and chemical potential, i.e., in Fig. 7, the multicritical point L where the C, SIC, and $OH1$ phases meet is located at

$$\begin{aligned} \mu_L &= C_A/2, \\ \varepsilon_L &= \frac{(k_B T_L)^2}{a_\perp^2 C''_B} = (2eg)^2 \exp\left[\frac{4I_{O1}}{k_B T_L}\right](2C_B - C_A). \end{aligned} \tag{18}$$

The quantity at the left-hand side of this equation is a suitable measure of temperature, and will be called ε. In the chiral 3-state Potts model L is located at $\Delta = \frac{1}{2}$ and $\varepsilon_L = 3J(2eg)^2$. As expected the multicritical temperature increases with the tilt energy C''_B. The parameter $(2eg)^2$ characterizes the strength of the breathing entropy; later, in Section 4, breathing entropy will turn out to be very weak in uniaxial systems, expecially with respect to meander entropy. The multicritical temperature is proportional to the elastic energy needed to transform one A wall into two B walls. Recall that $C_A = 2C_B$ is precisely the border line case where the A and B walls are energetically equally favorable, see (3).

Breathing entropy has to compete with three types of energy: the intersection energy, the elastic energy of the walls, and the tilt energy. The intersection energy I_O only renormalizes the strength $(2eg)^2$ of the breathing entropy, similar to the isotropic case where breathing stabilizes an intermediate HIC phase between the C solid and SIC solid at all finite temperatures, even if the intersection energy is positive and large. The tilt energy C''_B sets the temperature scale ε. The difference in compression energies $2C_B - C_A$ determines the threshold temperature below which the *OH* phase cannot exist. Breathing entropy is not able to compensate the energy needed to split one *A* wall into two vertical *B* walls below the multicritical point *L*. This is one of the intrinsic differences between uniaxial and isotropic networks. *OH* uniaxial networks contain two different types of walls, *A* and *B*, whose energies (at zero tilt angle) do not change sign simultaneously as a function of the chemical potential μ, see (3). Isotropic networks contain only one type of wall, the walls in the three easy directions are all of the same type, and therefore *L* is located at zero temperature.

This reason for the absence of the *OH* phase at very low temperatures can be circumvented. It is possible to construct a different honeycomb network, which still benefits from breathing entropy, but is built with only one type of wall. Such a phase could become stable at very low temperatures. The *XH* networks of Figs. 1c–d have that property and are discussed in Section 5.

How does the location of the multicritical point *L* relate to other characteristic temperatures of the system? The multicritical point *P* is associated with the C melting point in the absence of chirality. In the chiral Potts model it is located at $\Delta = 0$. *P* is the point where the C, *OH*1, and *OH*2 phases meet. Within our approximation the C solid does not melt; there are no dislocations; but the coexistence line between the *OH*1 and *OH*2 phases can be viewed as representing the C fluid phase, because there chirality cancels out, and the C fluid will appear. Within our approximation, the C solid "melts" at *P*, because the gain in breathing entropy becomes larger than the loss in energy needed to create domain walls and intersections.

When the intersection energies I_{O1} and I_{O2}, and also the tilt energies C''_A and C''_B are equal, e.g., in the chiral 3-state Potts model, *P* is the point along the C-*OH*1 coexistence line where $a = b/2$, i.e.,

$$\begin{aligned} b &= 2a, \\ \alpha 4ac &= \exp[-2-2d], \end{aligned} \tag{19}$$

where $\alpha = (1+x)^3/(2x^2)$, with $x = S_T/S_V = (\sqrt{17}-1)/8$, see (15), and $\alpha = 8.82$. This point will be labeled $\tilde{P}$, to distinguish it from *P* in the more general case where the two points do not coincide. The location of $\tilde{P}$ in terms of *T* and μ follows from (10):

$$\begin{aligned} \mu_{\tilde{P}} &= C_A - C_B, \\ \varepsilon_{\tilde{P}} &= \frac{(k_B T_{\tilde{P}})^2}{a_\perp^2 C''_B} = \alpha(2eg)^2 \exp\left[\frac{4I_{O1}}{k_B T_{\tilde{P}}}\right](2C_B - C_A). \end{aligned} \tag{20}$$

ε is the same measure for temperature as in (18). In the chiral Potts model *P* is located at $\Delta = 0$, $\varepsilon_P = 3J\alpha(2eg)^2/2$.

ε_P and ε_L differ by a factor of α; the minimum temperature ε_L where the *OH* phase exists is indeed linked to the C melting temperature. Therefore we must pay attention to the possibility that the *OH* network does not exist as a solid phase, but only as an OH fluid. If ε_L and ε_P are close, dislocations will likely melt the OH phase into an IC fluid. In the next section we show that this is almost certainly the case when meander entropy is included in the description of the OH phases. It turns out that around L and P meander entropy is very much larger than breathing entropy, by a factor of $(2eg)^2 \sim 100$, and that therefore ε_L and ε_P are much closer to each other than the factor α.

It is useful to compare the phase diagram of Fig. 7c with the one suggested for the chiral 3-state Potts model, Fig. 4. It is tempting to associate our multicritical point L with the Lifshitz point. Both points act as boundaries between regions where the system uses both types of wall and where it only realizes one type. If this identification is correct, then our calculation implies that at the chiral melting transition the C solid melts into an IC fluid which is not striped-like, but OH-like.

The competition between the C fluid and the chiral fluid determines how the C solid melts at small chirality. The breathing entropy associated with a local OH network might be the essential type of entropy which stabilizes the chiral fluid with respect to a SIC and C fluid. Consider a SIC phase which is a mixture of the two types of wall. Since one of the walls is still energetically more favorable, this mixture can only be lower in free energy with respect to a SIC phase containing only cheaper walls, by means of the entropy associated with transformations between the two wall types. There are three types of transformation mechanisms: intersections like in the OH phase (Fig. 3a), pair creation/annihilations (Fig. 3b), and intersections like in the XH phase (Fig. 3c). If the latter two do not destroy the character of the OH phase near the chiral melting transition, the IC fluid at the chiral melting will be an OH-type fluid. More detailed calculations including all three wall transformations mechanisms must be performed to clarify this point.

4. MEANDER EXCITATIONS IN OH-PHASES

In the previous section only the breathing entropy is accounted for. Breathing is the dominant type of entropy at very low temperatures, because it concerns modes which do not increase the energy of the honeycomb network. However, the temperature scale is set by the value of the tilt energy C''_B, which, as shown below, is strongly temperature dependent itself, and dominated by meander entropy. Moreover, it turned out that OH phases are not stable at low temperatures. At higher temperatures it is essential to include the other types of entropy, e.g., meander entropy, local fluctuations in the position of the intersection points and size of the top angles, and imperfections in the network (dislocations). Within the approach of this paper it is not possible to incorporate all of them. However it is possible to account for meander excitations of domain walls.

Consider the rectangular cutoff lattice. The intersection points of the honeycombs are assumed to coincide with the lattice points of the cutoff lattice. In Section 3, the domain walls were assumed to be rigid rods joining these vertices. Now the domain walls will be allowed to meander between their end points; they can choose their own paths along the bonds of the cutoff lattice between the intersection points, see Fig. 8. The intersection points themselves are still assumed to form a rigid honeycomb network; they can breath, but their positions are not allowed to fluctuate otherwise. Also the top angles of the honeycombs are still rigid, i.e., not allowed to fluctuate locally.

As a first step to introduce meander entropy, the energy of each wall (3) is replaced by the free energy of such a domain wall between two fixed (but far apart) end points in the absence of any other wall. This is again similar to Villain's calculation for the isotropic case [5]. The free energy associated with macroscopic tilts of the walls is obtained by choosing non-vertical end points (see Fig. 8). This is done in Appendix B. The result is

$$f_A(\theta)=E_A(0)/k_BT-\frac{1}{a_{\parallel}}\left[\sqrt{t_A^2+\gamma^2}-\gamma\sinh^{-1}\left(\frac{\gamma}{t_A}\right)\right], \tag{21}$$

where $E_A(0)$ is the energy of a wall of type A in the uniaxial direction at zero tilt angle $\theta=0$, $\tan\theta=\gamma(a_{\perp}/a_{\parallel})$, and $t_A=2\exp[-E_{\perp}a_{\perp}/k_BT]$ is the meander probability with $E_{\perp}$ the energy of a wall of type A along a bond of the cutoff lattice orthogonal to the uniaxial direction. The logarithmic correction due to the finite length of the domain walls is neglected to keep the discussion simple (see (B6)). Otherwise it would entangle the meander and breathing entropies and make it impossible to factor out the breathing entropy in a simple form as in Section 3.

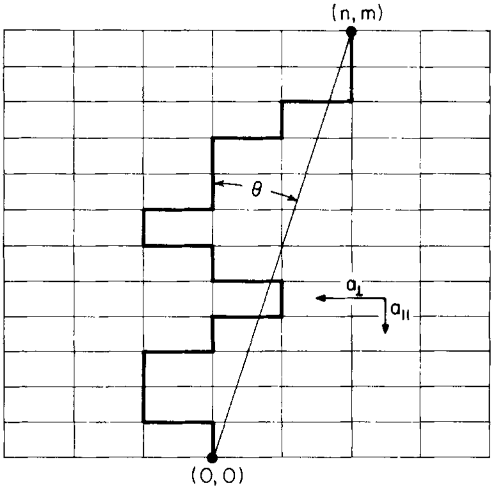

FIG. 8. Macroscopic tilt of meandering domain walls on a rectangular cutoff lattice with lattice constants $a_{\perp}$ and $a_{\parallel}$.

In the limit where the tilt is small with respect to the meander probability, $\gamma/t \ll 1$ (21) can be expanded as

$$f_A(\theta) = E_A(0)/k_B R - \frac{1}{a_\parallel}\left[t_A + \frac{\gamma^2}{2t_A} + O(\gamma^3/t_A^2)\right]. \tag{22}$$

Then the free energy of the OH phases has still exactly the same functional form as in the rigid wall case (11), but with new renormalized parameters. For the $OH1$ phase the μ and T dependences of a, b, c, and d change into

$$\begin{aligned} a &= E_A(0)/k_B T - t_A/a_\parallel = (C_A - 2\mu)/k_B T - t_A/a_\parallel, \\ b/2 &= E_B(0)/k_B T - t_B/a_\parallel = (C_B - \mu)/k_B T - t_B/a_\parallel, \\ c &= a_\parallel/(a_\perp^2 t_B), \\ d &= 2I_{O1}/k_B T + \ln(g\, a_\perp). \end{aligned} \tag{23}$$

The expressions for the parameters of the $OH2$ phase are similar.

Numerical calculation using (21) instead of (22) confirm that γ/t remains small at all temperatures. Notice that at zero temperature and/or $\gamma/t \gg 1$ the energy needed to tilt the wall becomes linear as $|\tan(\theta)|$ instead of quadratic. It is easy to check in Section 3, that a linear tilt energy would lead to a total absence of the HIC phases. The quadratic dependence on the tilt is essential for stabilizing the HIC phases. Therefore it is not surprising that γ/t remains much smaller than 1 at all temperatures.

This approximation for the meander entropy is not adequate however. It neglects the reduction in meander entropy caused by the presence of the other walls. Since domain walls are not allowed to cross each other, they reduce the freedom of each other to meander. This crowding effect is essential for the nature of the Pokrovsky–Tapalov (PT) transition between the C and SIC phases. To describe the SIC phases properly this crowding effect must be included in the free energies of the SIC phases, and then, in order to obtain a consistent description of the HIC–SIC boundaries, it must be included in the free energies of the HIC phases as well.

The top angle of the honeycombs is very small, and the local surroundings of each wall are very striped-like. Therefore, one way to incorporate crowding, is to treat the wall as if it is a part of a SIC phase. The free energy of a SIC phase of meandering walls is well known and easily calculated (e.g., see [1]).

$$f_{\mathrm{SIC}} = \frac{E_A(0)\, d_A}{k_B T} - \frac{t_A \sin(d_A \pi a_\perp)}{\pi a_\perp a_\parallel}, \tag{24}$$

where d_A is the density of walls of type A. For convenience the so-called tight binding approximation is used, where each individual wall excitation along the $a_\perp$ bonds is not allowed to be longer than one unit $a_\perp$ of the cutoff lattice. This is a valid approximation for highly uniaxial systems.

Equation (24) leads to the well-known PT transition between SIC and C solid phases. This is a second-order transition, i.e., d_A vanishes continuously. The crowding effect does not change the locations of C–SIC phase boundaries; the transition between the SIC phase with A walls and the C phase still takes place at $a=0$.

To introduce crowding into the description of the HIC phase, the wall-free energy (22) is replaced by the free energy of a wall in a SIC phase at a corresponding density,

$$f_A(\theta)=\frac{E_A(0)}{k_B T}-\frac{t_A \sin(d_A \pi a_\perp)}{d_A \pi a_\perp a_\parallel}+\frac{\gamma^2}{2a_\parallel t_A}. \tag{25}$$

For simplicity only the part associated with zero tilt is modified. The justification for this decoupling of the tilt energy and the crowding effect is that the tilt remains small. For the vertical walls in the OH network, the density d_V is chosen to be equal to the inverse of the average width of the honeycombs, $d_V=1/2S_T$. For the tilted walls, the density is chosen to be equal to $d_T=1/S_T$, because on the average the distance between the tilted walls is twice as large. Notice that (25) reduces to (22) in the limit of zero wall density.

The free energy per unit area for the $OH1$ network is now given as

$$\begin{aligned} f(S_T, S_V, \varphi)=\frac{\varphi}{2S_T(S_T+S_V)}\Bigg[& aS_V/\varphi+bS_T/\varphi+c\varphi S_T+d+\ln\left(\frac{1}{S_T}+\frac{1}{S_V}\right) \\ &+\frac{t_A S_V}{\varphi a_\parallel}\left(1-\frac{\sin(\pi a_\perp/2S_T)}{\pi a_\perp/2S_T}\right)+2\frac{t_B S_T}{\varphi a_\parallel}\left(1-\frac{\sin(\pi a_\perp/S_T)}{\pi a_\perp/S_T}\right)\Bigg]. \end{aligned} \tag{26}$$

The parameters a, b, c, and d are defined in (23). It should be stressed that the only purpose of (26) is to describe the $OH1$ and $OH2$ phases qualitatively, consistent with the simplest description (24) of SIC phases and with the correct order of magnitude of meander entropy versus breathing entropy.

Figure 9 shows how Fig. 7c changes due to the meander entropy and the crowding effect. The $OH1$ and $OH2$ phases virtually disappear! They are only realized in an extremely small region around the "Potts" multicritical point P, shown in Figs. 9b–c. The underlying reason for this collapse is that meander entropy is much larger than the breathing entropy at temperatures close to P and L. Meander entropy is $(2eg)^2 \sim 100$ times larger. Therefore breathing has only a minor effect on a phase diagram where HIC phases are ignored.

The $OH1$ and $OH2$ phases have flipped in position with respect to Fig. 7c. With crowding the $OH1$ phase appears to the left of the $OH2$ phase. As explained in Section 3, if the A walls are energetically more favorable than the B walls, one expects to find an $OH1$ phase with $x<\frac{1}{2}$, or an $OH2$ phase with $x>\frac{1}{2}$; x characterizes the ratio between the tilted and vertical wall lengths. Crowding introduces an effective repulsion between the walls and makes the $OH2$ phase with $x>\frac{1}{2}$ favorable.

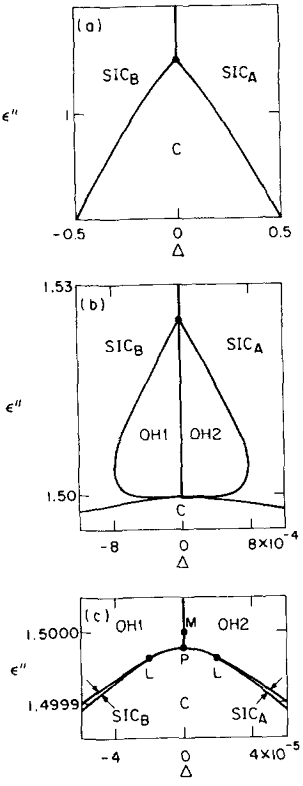

FIG. 9. Phase diagram of the chiral 3-state Potts model in the approximation with meandering domain walls. $\varepsilon'' = \varepsilon/J$ is used as the temperature scale and g is chosen to be equal to one. Details around the Potts melting point P are shown in (b) and (c).

The wall free energies are now temperature dependent, via the meander probabilities t_A and t_B, see (21)–(23). An isolated wall at zero tilt of type A (resp. type B) would melt, i.e., its surface tension as estimated by (21) becomes negative, at $a = 0$ (resp. $b = 0$). It is useful to choose $\varepsilon = t_B k_B T/a_\parallel$ as temperature variable. This is the same choice as in Section 3, because $C_B = k_B T a_\parallel/(a_\perp)^2 t_B$, see (10), (18), and (23). In Fig. 7 the lines $a = 0$, $b = 0$, and $a = b/2$ are parallel, but now they intersect (except for the special case $t_A = 2t_B$). The intersection point $a = b/2 = 0$ is called M, see Fig. 9c. It gives an estimate for the non-chiral Potts melting temperature when breathing entropy is neglected; $\varepsilon_M = (2C_B - C_A)/(2 - t_A/t_B)$. Similarly $\varepsilon_M = 3J/2$ in the chiral Potts model. Notice that ε_M has the correct order of magnitude compared to the exactly known location of the critical point in the non-chiral Potts model, i.e., $\varepsilon = J$ in the anistropy limit [13]. Notice that P and L are extremely close to M, see Fig. 9c. Compare this with the location of L and P in Section 3, (18) and (20). There ε_P and ε_L are predicted to be larger than here by a factor $(2eg)^2 \sim 100$. The factor $(2eg)^2$ measures the ratio between meander and breathing entropies. The multicritical point P in Fig. 9 is an estimate of the Potts non-chiral melting temperature including both meander and breathing entropy. Since breathing entropy is so small, P is located just below M.

This does not yet explain why L is also located very close to M. Recall that L is the multicritical point where the C, SIC, and $OH1$ phases meet. Also realize that (16) implies that L is the point along the line $a=0$ (the line where the surface tension of the vertical walls vanishes), where the ratio between the temperature and the surface tension of two tilted walls, ε_L/bk_BT, becomes larger than $(2eg)^2$ (apart from a renormalization due to the intersection energy). Only beyond this threshold, the breathing entropy compensates for the free energy needed to split vertical walls into tilted walls. Since the lines $a=0$ and $b=0$ approach point M linearly with different slopes, see (23), L must be located extremely close to M.

To illustrate this point further, ignore the crowding effect momentarily. Then (11) and (23) determine the free energy of the OH phases. The phase diagram would be the same as in Fig. 7, but highly deformed due to the renormalization of the parameters by meander entropy. Consider the triangle formed by the points P, L, and M. L is still given by (16), and P by (19). In the μ versus T phase diagram M, P, and L are now located at

$$\begin{aligned} \mu_M &= C_A - C_B - (t_A - t_B)\, k_B T_M/a_\parallel, \\ 2\mu_L &= C_A - t_A k_B T_L/a_\parallel, \\ \mu_P &= C_A - C_B - (t_A - t_B)\, k_B T_P/a_\parallel, \\ \frac{2C_B - C_A}{\varepsilon} &= \left(2 - \frac{t_A}{t_B}\right) + \frac{e^{-4I_{O1}/k_BT}}{\alpha(2eg)^2}, \end{aligned} \tag{27}$$

with $\alpha=1$ at L, $\alpha=8.82$ at P (as in Section 3), and $\alpha=\infty$ at M. Compare this with (18) and (20). The basic change is the appearance of the meander term $2-t_A/t_B$ on the right-hand side. This term dominates (except for the special case $t_A=2t_B$), because the constant $(2eg)^2$ in the breathing term is much larger than one. It illustrates explicitly that the ratio between meander and breathing entropy is $(2eg)^2$. Therefore the α dependence is very weak, and the triangle P–L–M indeed collapses into an extremely small part of the phase diagram. The crowding effect renormalizes the values of α by factors of hundreds larger and make the triangle even smaller.

This calculation confirms in a dramatic way the suggestion of the previous section; that the presence of an OH phase is linked to the C melting temperature. If an OH phase exists, it is more likely an IC fluid rather than an IC floating solid. Moreover, one might wonder whether it is possible to escape the conclusion that OH phases are completely absent. The obvious conclusion from this calculation is that there are no OH phases. Since the OH network is a likely candidate for the backbone of the IC fluid at the chiral melting transition, and L a candidate for the Lifshitz point, this raises the question of the nature and presence of chiral melting. Although there is some debate about the location of the Lifshitz point in the chiral 3-state Potts model [13–18], there is strong numerical evidence that it is well separated from P [13, 14, 18]. Recall that in our approximation L is extremely close to P. L is the point along the $a=0$ line where bk_BT/ε becomes less than approximately 10^{-2}. Also in our calculation L would move away from P if the $a=0$ and $b=0$ lines do not cross at P linearly but approach each other much faster, e.g., as $\exp(-1/\Delta)$. The entropies that are not yet included, could renormalize the surface tensions of the two types of walls, a and b, in this manner. The fact that our approximation for the Potts critical point P is still a factor $\frac{3}{2}$ larger than the exact value, indicates that these other entropies must bend the $a=0$ and $b=0$ lines further considerably. So our calculation does not exclude the identification of L with the Lifshitz point, and the possibility of chiral melting from the C solid into (a very thin slice of) the OH fluid. Moreover, series expansions for the two surface tensions are available [13] and confirm that the lines $a=0$ and $b=0$ almost coincide until $\Delta \approx \frac{1}{4}$. In [13], the location of L was actually characterized numerically as the point where these two lines start to diverge significantly.

5. *XH*-TYPE HONEYCOMB NETWORKS

In this section the possibility of an intermediate XH-type honeycomb phase (Figs. 1c–d) between the C solid and SIC floating solid phases is discussed. Physical intuition tells one that the extremely sharp angles between the walls at the intersections must lead to high intersection energies, and may tempt one to disregard XH networks without further discussion, as too costly with respect to the SIC phase. However, Villain pointed out for isotropic networks that breathing entropy stabilizes an intermediate HIC phase between the C solid and SIC floating solid all the way to zero temperature, irrespective of the strength of the (positive) intersection energy. Moreover, this intersection energy is equal to zero in the conventional chiral 3-state Potts model with only nearest neighbor interactions between spin pairs.

In the isotropic case, the strength of the intersection energy determines the width of the HIC phase and the size of the jump in the domain wall density at the C–HIC transition, but does not prevent the HIC phase from extending to zero temperature. The discussion of anisotropic OH-type networks in Sections 3 and 4 confirms this. The only reason why the $OH1$ phase does not extend to zero temperature and the multicritical point L is located at finite temperature, is that in OH-type networks the vertical and tilted walls must be of a different type and therefore have different energies. This is circumvented with the construction of the XH networks where all walls are of the same type.

The presence of such an intermediate XH phase would contradict the accepted phase diagrams of uniaxial systems, where the possibility of HIC phases has not been considered before, but where it is believed that at low temperatures a direct transition from the C solid into the SIC solid takes place and that this is a Pokrovsky–Talapov transition. If no good reasons turn up for the absence of an intermediate XH phase, the conventional phase diagrams of uniaxial systems might have to be modified. On the other hand, if such reasons turn up, it better does not apply to isotropic systems because that would shake up the conventional phase diagram for isotropic systems.

The discussion will be restricted to the *XH*1 phase. The *XH*2 phase replaces the *XH*1 phase, if the *B*-type walls are energetically more favorable than the *A*-type walls, but the results are completely analogous. The free energy of the *XH* phases is approximated in the same way as the free energy of the *OH* phases in Sections 3 and 4.

The approximation for the breathing entropy of *XH* networks has exactly the same form as for *OH* networks (Appendix A); except that the tilt angle needs to be replaced by its complement, $\theta \to \pi - \theta$, and the average vertical honeycomb length l_V by the new average distance between intersections in the uniaxial direction, $l_V \to l_V - 2l_T \cos(\theta)$, see Fig. 6b. Therefore the free energy of the *XH*1 phase in the rigid wall approximation satisfies (11) with

$$\begin{aligned} a = b/4 &= E_A(0)/k_B T = (C_A - 2\mu)/k_B T, \\ c &= C''_A/k_B T, \\ d &= 2I_{X1}/k_B T + \ln(g a_\perp). \end{aligned} \tag{28}$$

The results of Section 3 can be transcribed to the *XH*1 phase. Figure 10 replaces Fig. 7a. Indeed the intermediate *XH*1 phase separates the C and the SIC phases completely to zero temperature. From (16) with $a = b/4$ it follows that the multicritical point where the C, SIC, and *XH*1 phases meet is located at zero temperature. The C–*XH*1 transition is first-order, see (15). The multicritical point *L* is now the point where the C, *OH*1, and *XH*1 phases meet. It has moved, but since meander entropy will have such a large effect on its location (see Sect. 4), there is no need to pay much attention to its location yet. The ratio $x = S_T/S_V$, which

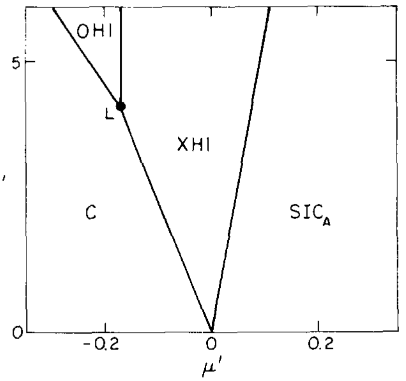

FIG. 10. Phase diagram in the rigid domain wall approximation with both the *XH* and *OH* phases when $C''_A = C''_B$ and $I_{01} = I_{X1} = 0$. The temperature and chemical potential are in the same units as in Fig. 7a.

characterizes the ratio between the tilted and vertical honeycomb lengths, is constant along the C–$XH1$ phase boundary, $x=(\sqrt{33}-1)/16=0.2965$, see (15). Therefore the equation of the C–$XH1$ phase boundary is simple,

$$\varepsilon=\frac{(k_BT)^2}{a_\perp^2\,C_A'}=\alpha(2eg)^2\exp\left[\frac{4I_{X1}}{k_BT}\right]E_A(0), \tag{29}$$

where $E_A(0)=C_A-2\mu$ or given by (5) in the chiral 3-state Potts model language and where $\alpha=(1+x)^3/(2x^2)=12.39$. As in Section 3, ε is a measure of temperature. The parameter $(2eg)^2$ characterizes again the strength of the breathing entropy, and the intersection energy I_{X1} again only renormalizes it.

Meander excitations are incorporated in the same way as in OH networks, see Section 4. First, the wall energy is replaced by the free energy of an isolated meandering wall (21)–(22). In that approximation the free energy is still given by (11), but with

$$\begin{aligned} a=b/4&=E_A(0)/k_BT-t_A/a_\parallel=(C_A-2\mu)/k_BT-t_A/a_\parallel,\\ c&=a_\parallel/(a_\perp^2\,t_A),\\ d&=2I_{X1}/k_BT+\ln(g\,a_\perp). \end{aligned} \tag{30}$$

Again, this only deforms the phase diagram. It tilts the $a=0$ line, but does not affect the presence of the $XH1$ phase nor does it change its width,

$$\frac{C_A-2\mu}{\varepsilon}=1+\frac{1}{\alpha(2eg)^2}\exp\left(-\frac{4I_{X1}}{k_BT}\right), \tag{31}$$

with $\alpha=12.39$ on the C–$XH1$ boundary, and $\alpha=\infty$ on the $a=0$ line. As in Section 4, we choose $\varepsilon=t_Ak_BT/a_\parallel$. Notice that (31) is basically the same as (29). The extra term on the right-hand side only reflects the tilt of the $a=0$ line due to meander entropy. This tilt is large with respect to the width of the XH phase, i.e., the second term is small relative to the first term because $(2eg)^2\sim 100$. This confirms again that the meander entropy is much stronger than the breathing entropy.

The $XH1$ phase is extremely narrow up to the melting temperature. The $XH1$ phase only includes one type of wall, and therefore has no knowledge about typical temperatures like the C melting temperature and the location of L, because those temperatures involve the energies of all types of walls. However, typically the compression energies of the other walls are of the same order of magnitude. So typically C melting takes place at a temperature ε of order C_A due to the meander entropy (see Sect. 4). There the width of the XH phase is only of order $(2eg)^{-2}\sim 10^{-2}$.

It is essential to incorporate the crowding effect, to obtain a proper description of the SIC phase and XH–SIC phase boundary. Also this is done in the same way as in Section 4, see (24)–(26). The only difference is that the average domain wall density in the regions with tilted walls is two times larger than in OH networks,

$$f(S_T, S_V, \varphi)=\frac{\varphi}{2S_T(S+S_V)}\left[a\,S_V/\varphi+4a\,S_T/\varphi+c\varphi S_T+d+\ln\left(\frac{1}{S_T}+\frac{1}{S_V}\right)\right.$$
$$\left.+\frac{t_A S_V}{\varphi a_\parallel}\left(1-\frac{\sin(\pi a_\perp/2S_T)}{\pi a_\perp/2S_T}\right)+4\frac{t_A S_T}{\varphi a_\parallel}\left(1-\frac{\sin(\pi a_\perp 2/S_T)}{\pi a_\perp 2/S_T}\right)\right]. \tag{32}$$

Crowding increases the free energy of both the XH and SIC phases. Therefore it is not surprising that the C–$XH1$ phase boundary moves closer to the $a=0$ line. The phase boundaries are given by (31) with $\alpha=5.22\times10^8$ on the C–$XH1$ boundary and $\alpha=-1.06\times10^2$ on the $XH1$–SIC boundary. As in Section 4, crowding renormalizes the values of α enormously.

The C–XH and XH–SIC transition are still first order, and the jumps in the order parameters remain extremely small: $x=0.484$ on the C–$XH1$ boundary and $x=32.7$ on the $XH1$–SIC boundary, and

$$\begin{aligned}\frac{a_\perp}{S_T}&=\omega_1\frac{\exp(-2I_{X1}/k_BT)}{(2eg)},\\ \varphi\frac{a_\parallel}{a_\perp t_A}&=\omega_2\frac{\exp(-2I_{X1}/k_BT)}{(2eg)},\end{aligned} \tag{33}$$

with $\omega_1=6.52\times10^{-5}$ and $\omega_2=3.57\times10^{-4}$ on the C–$XH1$ boundary, and $\omega_1=2.22\times10^{-2}$ and $\omega_2=2.20\times10^{-2}$ at the $XH1$-side of the $XH1$–SIC boundary. The wall density at the SIC side of the $XH1$–SIC boundary, $a_\perp/2S_T$ is given by (33) with $\omega_1=8.75\times10^{-2}$. The width of the $XH1$ phase becomes smaller only by a factor of 15 due to the crowding effects. Moreover the $XH1$ phase extends still to zero temperature!

What can we conclude about the possibility of an intermediate XH phase? The XH phase is indeed realized in these approximations, but is so narrow that it is unclear whether it survives when the approximations for the breathing and meander entropies are improved, and/or the remaining types of entropy are included. This must be addressed in the future by detailed quantitative calculations, using, e.g., transfer matrices or Monte Carlo simulations. If the XH phase survives, but remains very narrow with order parameters this small, it might be unobservable. Maybe the XH phase only survives above a new type of Lifshitz point.

If the XH phase does not survive, this calculation still suggests that the SIC phase becomes soft with respect to the formation of dislocations at the C–SIC phase boundary. This may change the Pokrovsky–Talapov (PT) nature of the C–SIC phase boundary. From the SIC phase point of view the XH phase is a dislocation network. The dislocation core energy I_X may be very large, but this is compensated by breathing entropy if the dislocations cluster into local XH networks. The theory leading to the prediction of the PT nature of the C–SIC transition assumes that the dislocation density is small. The PT transition fixed point is located at infinite dislocation core energy. It has been shown by renormalization group arguments that dislocations are an irrelevant perturbation in this limit of infinite core energy. The breathing entropy softness suggests a possible crossover at finite core energies to a new fixed point at large dislocation density, with a different type of C–SIC transition, probably first order.

The enormous difference in strength between breathing and meander entropy causes the *XH* phase to be very narrow. This is specific to uniaxial systems. The crucial difference between uniaxial and isotropic systems is that, in addition to intersection energy and wall energy, a tilt energy must be paid to form the honeycomb network. Breathing entropy is strong enough to compensate this tilt energy, but the *XH* phase is very narrow compared to the isotropic HIC phase. Villain's approximation for the breathing entropy in isotropic networks [5], can also be cast into the same form, (6). Therefore this free energy also is given by (11); but with fixed tilt angle, $\varphi = \tan(\pi/3)$; with tilt energy $c = 0$; and with $b = 2a/\cos(\pi/3)$. Then $x = S_T/S_V = \sqrt{a/b} = \cos(\pi/3)$. The C–HIC phase boundary is given by

$$k_B T/a_\perp = \frac{(1+x)^2}{2x^2}\,\frac{(2eg)}{\varphi}\exp[2I/k_B T]\;E_A(0), \tag{34}$$

in the rigid wall approximation, and by

$$\frac{C_A - 2\mu}{k_B T t_A/a_\parallel} = 1 + \frac{2\varphi}{a_\perp t_A/a_\parallel}\left(\frac{x}{1+x}\right)^2 \frac{1}{2eg}\exp[-2I/k_B T], \tag{35}$$

if the meander entropy is included in the wall-free energy, but crowding is still neglected. This is a bad approximation, because in (21), see Appendix B, the walls are only allowed to meander by one unit $a_\perp$ in each step. In isotropic systems the meander entropy is certainly larger. Moreover (35) is sufficient to illustrate the difference in temperature dependence between meander and breathing entropies in isotropic and uniaxial systems.

Compare the rigid wall approximations (34) and (29). Along the C–HIC phase boundary the chemical potential is linear in the temperature in isotropic systems but quadratic in uniaxial systems. So in the rigid wall approximation, the *XH* phase in uniaxial systems is already much narrower than the HIC phase in isotropic systems.

Compare (35) with (31). At low temperatures, the meander term on the right-hand side in (35) is not large with respect to the breathing term. The ratio between them is strongly temperature dependent, as $1/t_A$, and diverges at zero temperature. Therefore the C–HIC phase boundary remains linear in the temperature at very low temperatures. In (31), on the other hand, the meander term dominates over the breathing term at all temperatures. Therefore the C–*XH* phase boundary sticks to the $a = 0$ line and behaves exponentially at low temperatures. This difference in behavior originates from the temperature dependence of the tilt angle via the tilt energy. The tilt energy C''_A is dominated by the meander entropy and diverges exponentially at zero temperature.

So in uniaxial systems the XH phases are stable, within our generalization of Villain's theory for isotropic systems, but they are much narrower than in isotropic systems because, due to the tilt free energy, the breathing entropy is much weaker relative to the meander entropy than in isotropic systems.

APPENDIX A: BREATHING ENTROPY IN UNIAXIAL SYSTEMS

In this appendix we obtain an approximation of the breathing entropy of uniaxial honeycomb networks with a small tilt angle θ. The object is to find an approximation for the number of configurations that can be obtained by breathing each semi-regular honeycomb network. Figure 6 shows our notation for the angles and sides of the honeycombs. Our approximation is a direct extension of the one obtained by Villain [5] for isotropic networks.

Consider the breathing distances d_i of neighboring intersections in the semi-regular honeycomb network, see Fig. 5. The index i denotes the axis along which d_i is measured. In contrast to the isotropic case the d_i are different in different directions. The three directions are $i = V$, R, and L. It is also convenient to introduce the breathing distance $d_\perp$ perpendicular to the uniaxial (easy) direction V.

Because of the rigidity of the walls these four breathing distances are related as

$$\frac{d_V}{\sin(\theta_V)} = \frac{d_R}{\sin(\theta_R)} = \frac{d_L}{\sin(\theta_L)} = \frac{d_\perp}{\sin(\theta_L)\sin(\theta_R)}. \tag{A1}$$

Their values are restricted by the requirement that the sides of the honeycombs must remain positive. A sufficient but not necessary condition for this is

$$\frac{d_V}{\sin(\theta_V)} = \frac{d_\perp}{\sin(\theta_R)\sin(\theta_L)} < \frac{1}{4}\left|\frac{l_i}{\sin(\theta_i)}\right|, \tag{A2}$$

for $i = V$, R, and L, and assuming that θ_R and θ_L are larger than $\pi/2$.

This condition gives a lower bound to the number of breathing modes, by dividing this estimate for the maximum breathing length by the lattice cutoff $a_\perp$. This brings into the discussion a new aspect, which is absent in the isotropic case: The breathing distance along one axis is in general not a simple rational multiple of the d_i along the other axes. A breathing distance which matches the cutoff lattice along one direction does not necessarily match in other directions. All four d_i must be lattice vectors of the cutoff lattice simultaneously, because all intersections must coincide with lattice points of the cutoff lattice. If we take this seriously, we must conclude that the breathing entropy is a highly irregular discontinuous function of the tilt angle θ. For simple rational values of the angle the entropy will be large, but for nearby higher order rational values the entropy will almost vanish, because the d_i almost never match. Fortunately we do not have to worry too much about this esoteric behavior. Apart from the fact that it will smooth out as soon as meander excitations in the walls are allowed, it turns out not to be important at small tilt angles. Consider the sequence of angles for which it is true that if $d_\perp$ is a lattice vector of the cutoff lattice, all other three d_i lock-in automatically. It is easy to see that this set becomes dense in the limit of small tilt angle. So although strictly speaking we will restrict ourselves to this set, we can treat θ as a continuous variable.

All breathing configurations can now be counted by the number of times when $d_\perp$ becomes equal to a lattice vector in the interval given by (A2). The lower bound (1b) estimate of the number of breathing modes is

$$g_{\text{breath}}^{(1b)} = \left(\frac{2d^{(\max)}}{a_\perp}\right)^{v}, \tag{A3}$$

where v is the total number of honeycombs, $d^{(\max)}$ is the maximum breathing length which satisfies all three conditions (A2), and $a_\perp$ the lattice constant of the rectangular cutoff lattice. Following Villain we replace (A3) by a form which removes the need to solve Eq. (A2) first. Using the inequality $\min(a, b, c) \geqslant (1/a + 1/b + 1/c)^{-1}$ we find

$$g_{\text{breath}}^{(1b)} \geqslant \left[2a_\perp\left(\frac{1}{1_L \sin(\theta_R)} + \frac{1}{l_R \sin(\theta_L)} - \frac{1}{l_V}\left(\frac{1}{\tan(\theta_L)} + \frac{1}{\tan(\theta_R)}\right)\right)\right]^{-v}. \tag{A4}$$

It is noteworthy that Villain's approximation for isotropic networks transform into (A4) by

$$\begin{aligned} l_L &\to l_L \sin(\theta_R), \\ l_R &\to l_R \sin(\theta_L), \\ l_V &\to -l_V[1/\tan(\theta_R) + 1/\tan(\theta_L)]^{-1}, \end{aligned} \tag{A5}$$

which are precisely the scale factors needed to distort an isotropic honeycomb into the uniaxial honeycomb.

In addition to the lower bound, Villain also constructed an upper bound approximation for the breathing entropy. It only differs from the lower bound by a factor g of order unity. We assume, because of the scale factors (A5), that this is also the case for the uniaxial network.

In the text of this paper we restrict ourselves to the special case where the R and L walls are of the same type, i.e., where $\theta_R = \theta_L$ and $l_R = l_L = l_T$. Then (A4) reduces to (6) in Section 3. The precise value of the constant g is unknown, but is not crucial for our discussion. In the lower bound approximation $g = 4$. It must be stressed that (A4) can only be expected to be a reasonable approximation to the true breathing entropy in the limit of large honeycombs (large with respect to the cutoff) and small tilt angles.

The derivation of the approximation of the breathing entropy of the X-type honeycomb networks is similar. The breathing entropy has exactly the same form (6), except that θ now refers to the outside angle, i.e., $\theta \to \pi - \theta$, and that l_V does not refer anymore to the average vertical side length of the honeycomb, but to $l_V \to l_V - 2l_T \cos(\theta)$ (see Fig. 6b).

APPENDIX B: FREE ENERGY OF A SINGLE DOMAIN WALL

In this appendix we derive the free energy of an isolated single meandering domain wall between two fixed, but far apart end points. The wall follows the bonds of the rectangular cutoff lattice (see also Section 3). We use the transfer matrix method. A similar calculation has already been done by Villain [5]. We repeat it here, because we need to concentrate on the tilt free energy, which is obtained by introducing a tilt angle between the two end points with respect to the uniaxial direction.

The partition function $Z(n, m)$ of a string that starts at site $r = (0, 0)$ and ends at site $r = (na_\perp, ma_\parallel)$, see Fig. 8, satisfies the recurrence relation

$$Z(n, m) = \sum_{j=-1,0,1} Z(n+j, m-1) \exp[-(E_\parallel a_\parallel + E_\perp a_\perp j)/k_B T], \tag{B1}$$

where $E_\parallel$ is the energy of the wall along the bonds in the uniaxial direction, and $E_\perp$ its energy orthogonal to the uniaxial direction. The summation can be restricted to nearest neighbours, because $E_\parallel \ll E_\perp$ in uniaxial systems. The initial partition function in row $m=0$ is equal to $Z(n, 0) = \delta(n, 0)$.

By Fourier transformation of the n coordinate,

$$Z(n, m) = \frac{1}{2\pi} \int_{-\pi}^{\pi} Z(k, m) \exp(ikn)\, dk, \tag{B2}$$

(B1) diagonalizes,

$$\frac{Z(k, m)}{Z(k, m-1)} = \exp(-E_\parallel a_\parallel/k_B T)[1 + 2\cos(k) \exp(-E_\perp a_\perp/k_B T)]. \tag{B3}$$

Since the meander probability $t = 2\exp(-E_\perp a_\perp/k_B T)$ is very small, the partition function can be approximated by

$$Z(\gamma, m) \approx \frac{1}{2\pi} \exp(-m\, E_\parallel a_\parallel/k_B T) \int_{-\pi}^{\pi} \exp[m(ik\gamma + t\cos(k))]\, dk, \tag{B4}$$

where $\gamma = n/m$ relates to the tilt angle θ as $\tan(\theta) = \gamma(a_\perp/a_\parallel)$. Using the steepest descent method, we obtain for large m

$$Z(\gamma, m) \approx \exp(-m\, E_\parallel a_\parallel / k_B T)(8\pi m)^{-1/2}(t^2+\gamma^2)^{-1/4} \times \exp\left[m\left(\sqrt{t^2+\gamma^2} - \gamma \sinh^{-1}\left(\frac{\gamma}{t}\right)\right)\right]. \tag{B5}$$

We measure wall lengths by their projection along the vertical direction. For very large wall lengths $ma_\parallel$, the free energy of a single domain wall with macroscopic tilt angle θ is equal to $f = -\log Z/(a_\parallel m)$, i.e.,

$$f = \frac{E_\parallel}{k_B T} - \frac{1}{a_\parallel}\left[\sqrt{t^2+\gamma^2} - \gamma \sinh^{-1}\left(\frac{\gamma}{t}\right) - \lim_{m\to\infty} \frac{\ln m}{2m}\right], \tag{B6}$$

which reduces in the limit of infinite wall length to (21) in Section 4. Notice that the lowest order finite length correction is logarithmic.

ACKNOWLEDGMENTS

This research was supported in part by the National Science Foundation under Grants DMR 83–19301 and DMR 85–09392. One of us (H.P.) acknowledges support from the University of Washington Graduate School Research Fund.

REFERENCES

1. J. Villain, *in* "Ordering in Strongly Fluctuating Condensed Matter Systems" (T. Riste, Ed.), p. 221, Plenum, New York, 1980.
2. P. Bak, *Rep. Prog. Phys.* **45** (1982), 587.
3. P. Bak, D. Mukamel, J. Villain, and K. Wentowska, *Phys. Rev. B* **19** (1979), 1610.
4. V. L. Pokrovsky and A. L. Talapov, *Phys. Rev. Lett.* **42** (1979), 65.
5. J. Villain, *Surf. Sci.* **97** (1980), 219.
6. S. N. Coppersmith, D. S. Fisher, B. I. Halperin, P. A. Lee, and W. F. Brinkman, *Phys. Rev. Lett.* **46** (1981), 549; *Phys. Rev. B* **25** (1982), 349.
7. R. J. Gooding, R. Joos, and B. Bergersen, *Phys. Rev. B* **27** (1983), 7669.
8. F. F. Abrahams, W. E. Rudge, D. J. Auerbach, and S. W. Koch, *Phys. Rev. Lett.* **52** (1984), 445.
9. C. Peters and M. L. Klein, preprint, 1985.
10. M. Kardar and R. Shankar, *Phys. Rev. B* **31** (1985), 1525.
11. S. Ostlund, *Phys. Rev. B* **24** (1981), 398.
12. M. Kardar and A. N. Berker, *Phys. Rev. Lett.* **48** (1982), 1552.
13. S. F. Howes, *Phys. Rev. B* **27** (1983), 1762.
14. S. F. Howes, L. P. Kadanoff, and M. P. M. den Nijs, *Nucl. Phys. B* **215** (1983), 169.
15. H. J. Schulz, *Phys. Rev. B* **28** (1983), 2746.
16. F. D. M. Haldane, P. Bak, and T. Bohr, *Phys. Rev. B* **28** (1983), 2743.
17. D. A. Huse and M. Fisher, *Phys. Rev. B* **29** (1984), 239.
18. W. Selke and J. M. Yeomans, *Z. Phys. B* **46** (1982), 311.
19. S. C. Fain, Jr., M. D. Chinn, and R. D. Diehl, *Phys. Rev. B* **21** (1980), 4170.

20. R. D. DIEHL AND S. C. FAIN, JR., *Phys. Rev. B* **26** (1982), 4785.
21. A. D. MIGONE, H. K. KIM, M. H. W. CHAN, J. TALBOT, D. J. TILDESLEY, AND W. A. STEELE, *Phys. Rev. Lett.* **51** (1983), 192.
22. P. W. STEPHENS, P. A. HEINEY, R. J. BIRGENEAU, P. M. HORN, D. E. MONCTON, AND G. S. BROWN, *Phys. Rev. B* **29** (1984), 3512.
23. K. L. D'AMICO, D. E. MONCTON, E. D. SPECHT, R. J. BIRGENEAU, S. E. NÄGLER, AND P. M. HORN, *Phys. Rev. Lett.* **53** (1984), 2250.
24. H. YOU AND S. C. FAIN, JR., *Surf. Sci.* **151** (1985), 361.
25. P. R. KUBIK, W. N. HARDY, AND H. GLATTLI, *Canad. J. Phys.* **63** (1985), 605.
26. R. IMBIHL, R. J. BEHM, K. CHRISTMANN, G. ERTL, AND T. MATSUSHIMA, *Surf. Sci.* **117** (1982), 257.
27. K. H. RIEDER, *Phys. Rev. B* **27** (1983), 7799.
28. I. P. BATRA, T. ENGEL, AND K. H. RIEDER, *in* "The Structure of Surfaces" (M. A. van Hove and S. Y. Tong, Eds.), p. 251, Springer, Berlin, 1985.
29. C. NÖBL, C. BENNDORF, AND T. E. MADEY, *Surf. Sci.* **157** (1985), 29.
30. M. JAUBERT, A. GLACHANT, M. BIENFAIT, AND G. BOATO, *Phys. Rev. Lett.* **46** (1981), 1679.